



Physical Modulation to the Biological Productivity in the Summer Vietnam Upwelling System

Wenfang Lu^{1,2,3,4}, Enhui Liao^{2,3,4,6}, Xiao-Hai Yan^{3,4}, Lie-Yauw Oey^{5,6}, Wei Zhuang^{2,4}, Yuwu Jiang^{2,4}

5 ¹Key Laboratory of Spatial Data Mining and Information Sharing of Ministry of Education, & National Engineering Research Centre of Geo-spatial Information Technology, Fuzhou University, Fuzhou, 350116, China

²State Key Laboratory of Marine Environmental Science, College of Ocean and Earth Sciences, Xiamen University, Xiamen, 361102, China

³Center for Remote Sensing, College of Earth, Ocean and Environment, University of Delaware, Newark, DE, USA

10 ⁴Joint Institute for Coastal Research and Management, University of Delaware/Xiamen University, USA/China

⁵National Central University, Jhongli City, Taoyuan County, Taiwan

⁶Princeton University, Princeton, New Jersey, USA

Correspondence to: Yuwu Jiang (ywjiang@xmu.edu.cn)

Abstract. Biological productivity in the summer Vietnam boundary upwelling system in the western South
15 **China Sea, as in many coastal upwelling systems, is strongly modulated by wind. However, the role of ocean**
circulation and mesoscale eddies has not been elucidated. Here we show a close spatio-temporal covariability
between primary production and kinetic energy. High productivity is associated with high kinetic energy,
which accounts for ~15% of the production variability. Results from a physical-biological coupled model
reveal that the elevated kinetic energy and intensified circulation can be explained by the separation of the
20 **upwelling current system. The separated current forms an eastward jet into the interior South China Sea,**
and the associated southern gyre traps nutrient and favors productivity. When separation is absent, the
model shows weakened circulation and eddy activity, with ~21% less nitrate inventory and ~16% weaker
primary productivity.



25 1 Introduction

The South China Sea (SCS) is a large semi-enclosed marginal sea located in the western Pacific Ocean (Fig. 1a). It is bordered by extensive continental shelves along the southern coast of China and northeastern Vietnam, and the Sunda Shelf south of Vietnam (Fig.1). It has a deep interior basin which can be as deep as 5000 m (Liu et al., 2010; Wong et al., 2007). The SCS is predominantly controlled by the East Asian Monsoon. The wind is southwesterly from June to September, and northeasterly from November to March (Liu et al., 2002). Because of efficient biological production, the interior SCS has low nutrient concentration in the euphotic zone, displaying a oligotrophic condition (Wong et al., 2007).

Coastal upwelling is one of the most important processes for ocean productivity and fishery (Gruber et al., 2011). During southwesterly monsoon, upwelling-favorable wind prevails along the southern coast of Vietnam over the complex topography (Fig. 1b). The offshore Ekman transport drives surface divergence, and results in coastal upwelling of cold and nutrient-rich subsurface water. We refer this as the Vietnam Boundary Upwelling System (VBUS). The VBUS is centered near $\sim 109^\circ$ E between 14° N and 17° N along the coast (Loisel et al., 2017). Upwelling in VBUS was confirmed by cruise (Dippner et al., 2006) and remote sensing observations (Kuo et al., 2000).

In VBUS, the upwelling intensity is governed by the strength of the alongshore monsoon wind, as in other coastal upwelling systems such as the coastal upwelling systems of California and mid-Atlantic Bight (Gruber et al., 2011). The VBUS upwelling strength is intense, and can result in surface cooling of $3\text{--}5^\circ\text{C}$ and an associated cold filament length of ~ 500 km (Kuo et al., 2004). The VBUS is modulated by different climatic variations, such as the El Niño and Southern Oscillation (Dippner et al., 2006; Hein et al., 2013; Xie et al., 2003), the Indian Ocean Dipole (Liu et al., 2012; Xie et al., 2009), and the Madden-Julian Oscillation (Isoguchi and Kawamura, 2006; Liu et al., 2012).

The nutrient balance and ecosystem in the VBUS are controlled by the El Niño variability which modulates the summer monsoon (Chai et al., 2009; Kuo and Ho, 2004). During post-El Niño summer, the weakened southwesterly wind weakens the upwelling and reduces the upward nutrient flux (Xie et al., 2003). In addition, Hein et al. (2013) proposed instead that productivity is controlled by lateral transport of nitrate in the VBUS. Liu et al. (2002) also highlighted the role of coastal jet located to south of Vietnam coast. They mentioned that jet-induced upwelling was responsible for the nutrient influx. These contradictory conclusions in previous works motivate us to examine the VBUS ecosystem and its connection with circulation.

Early hydrodynamic observations revealed a northeastward coastal current over the southern shelf of Vietnam (Wyrtki, 1961). The current separates and flows offshore at about 11°N (Xu et al., 1982). Xie et al. (2003) ascribed the jet separation to the strong wind jet off Vietnam due to orographic steering of the north-south running mountains. Using an idealized reduced gravity model, Wang et al. (2006) highlighted vorticity input by wind-stress curl and vorticity advection by the basin circulation. Gan and Qu (2008) found that the separation was associated with an adverse pressure gradient induced by the topographic effects.



60 The separated jet produces cooling and results in biannual SST variation in the SCS (Xie et al., 2003). The
offshore jet also appears to advect water with high chlorophyll (CHL) to the interior of the central SCS (Chen et al.,
2014; Loisel et al., 2017; Tang et al., 2004). While the importance of circulation to the VBUS biogeochemical
system has been noted in some previous studies (Dippner et al., 2006; Kuo et al., 2004; Liu et al., 2012; Xie et al.,
2003), the detailed processes are unclear. To what extent is the ecosystem in VBUS modulated by local circulation?
65 How does the coastal jet modulate productivity? How much does the local circulation contribute to production?
Studying biological production and its coupling with physical processes in the VBUS will help to answer these
questions and further improve the understanding of boundary upwelling system. Such a study will also shed light on
the ecosystem dynamic in the SCS as an oligotrophic marginal sea. Here we analyze the complex dynamics of the
VBUS using a physical-biological coupled numerical model system, as well as remote sensing data and *in situ*
70 observations.

This paper is organized as follows. In Sect. 2, model configuration, numerical experiments, observed data, and
statistical method used in this study are described. In Sect. 3, we analyze the remote sensing data and validate the
model. Model results from both the standard run and the sensitivity experiment are presented. In Sect. 4, the
dynamical processes are analyzed. Conclusions are given in Sect. 5.

75 2 Model, Data and Methods

2.1 Data

The surface wind vectors were from the Cross-Calibrated Multi-Platform (CCMP) gridded data. This is a 25-year,
six-hourly, $1/4^\circ \times 1/4^\circ$ resolution product fused from several microwave radiometers and scatterometers using a
variational analysis method (Atlas et al., 2011). Monthly Moderate Resolution Imaging Spectroradiometer (MODIS)
80 Aqua level-3 CHL (4 km resolution) was obtained from the NASA Distributed Active Archive Center. The
estimated monthly vertical-integrated net primary production (NPP) was derived from MODIS CHL data via the
standard chlorophyll-based Vertically Generalized Production Model (VGPM) algorithm (Behrenfeld and Falkowski,
1997). The VGPM NPP product had a resolution of $1/10$ degree, covering the period from 2004 to present. Gridded
monthly-mean Absolute Dynamic Topography (ADT) at $1/4^\circ$ resolution was acquired. The $1/4^\circ$ Optimum
85 Interpolation Sea Surface Temperature (OISST, also known as Reynolds 0.25v2) was constructed by combining the
Advanced Very High Resolution Radiometer satellite and other observation data (Banzon et al., 2016). *In situ*
observed nitrate and CHL profiles from the western SCS stations (Fig. 1b) were used, as detailed in Jiao et al. (2014).

2.2 Methods

2.2.1 Upwelling Intensity (UI) and Kinetic Energy (KE)

90 We use the upwelling intensity (UI) as a proxy to measure the strength of upwelling (Chen et al., 2012; Gruber et al.,
2011):



$$\mathbf{UI} = \frac{\tau_y}{\rho_0 f} = \frac{\rho_a C_D U_y |U_y|}{\rho_0 f}. \quad (1)$$

Here, τ_y is the along-shore component of wind stress, f is the Coriolis parameter, ρ_0 is sea water density (constant, 1025 kg m⁻³), ρ_a is the air density (constant, 1.2 kg m⁻³), C_D is the drag coefficient and U_y is the alongshore wind speed. The CCMP data with full temporal and spatial coverage close to the coastline is used for the wind speed.

The kinetic energy (KE) of the near-surface geostrophic current is used as an indicator of the circulation intensity. The near-surface geostrophic current is calculated from absolute dynamic topography (ADT) using the geostrophic balance. The KE then equals:

$$\text{KE} = \frac{1}{2}(u_g^2 + v_g^2) = \frac{1}{2\rho_0^2 f^2} \left[\left(\frac{\partial \text{ADT}}{\partial x} \right)^2 + \left(\frac{\partial \text{ADT}}{\partial y} \right)^2 \right], \quad (2)$$

100 2.2.2 Multivariable Linear Regression

Monthly net primary production (NPP) from VGPM (Vertically Generalized Production Model; see Sect. 2.1 Data) was used to estimate biological productivity. A multivariable linear regression analysis was conducted to examine the statistical relations among NPP, UI, and KE:

$$\text{NPP} = b_1 \text{UI} + b_2 \text{KE} + b_3, \quad (3)$$

105 where b_1 , b_2 and b_3 are parameters. Data in the summer months (MJJAS) were used since the monsoon wind during this period is upwelling-favorable. We averaged NPP and KE over the ocean region enclosed by the magenta ‘box’ off the coast of Vietnam (Fig. 2b). Only the summertime data in the overlapping period from 2004 to 2012 were analyzed. Contributions from SST, day length and the photosynthetically active radiation were implicitly considered in the VGPM (Behrenfeld and Falkowski, 1997).

110 2.3 Model Description

We use a three-dimensional general circulation model based on the Regional Ocean Model System (ROMS). ROMS is a free-surface and hydrostatic ocean model. It solves the Reynolds-averaged Navier-Stokes equations on terrain-following coordinates (Shchepetkin and McWilliams, 2005). The model is used in the operational Taiwan Strait Nowcast\Forecast system (TFOR), which successfully provides multi-purpose ocean forecasts (Jiang et al., 2011; Liao et al., 2013; Lin et al., 2016; Lu et al., 2017; Lu et al., 2015; Wang et al., 2013). In this study, the model grid is modified to cover the whole SCS domain and part of the North-Western Pacific with a grid resolution of 1/10 degree (Fig. 1a). The number of grid nodes in x and y direction are 382 and 500, respectively. In the vertical, 25 σ -levels is used with a grid size of ~ 2 m on average near the surface to resolve the surface boundary layer. Following the bulk



120 formulation scheme (Liu et al., 1979), daily atmospheric fluxes are applied at surface. The atmospheric forcing
includes downward shortwave radiation, downward longwave radiation, air temperature, air pressure, precipitation
rate and relative humidity, acquired from the National Centers for Environmental Prediction (NCEP) Reanalysis
data (<http://www.esrl.noaa.gov/psd/data/gridded/data.ncep.reanalysis.html>, Kalnay et al., 1996) distributed by the
NOAA/OAR/ESRL PSD, Boulder, Colorado, USA (<http://www.esrl.noaa.gov/psd/>). The wind vectors are from the
CCMP wind. The vertical turbulent mixing uses a K-profile parameterization (KPP) scheme (Large et al., 1994)
125 which was successfully applied in a one-dimensional vertical mixing model in the SCS (Lu et al., 2017). The KPP
scheme estimates eddy viscosity within boundary layer as the production of the boundary layer depth, a turbulent
velocity scale and a dimensionless third-order polynomial shape function. Beyond the surface boundary layer, KPP
scheme includes vertical mixing collectively contributed by shear mixing, double diffusive process and internal
waves. Biharmonic horizontal mixing scheme (Griffies and Hallberg, 2000) with a reference viscosity of 2.7×10^{10}
130 $\text{m}^4 \text{s}^{-1}$ is applied, following the value of Bryan et al. (2007) used in a circulation model with the same horizontal
resolution. Climatological river discharges from the Mekong River and other major rivers are included as point
sources.

The biogeochemical module is the Carbon, Silicon, Nitrogen Ecosystem (CoSINE) model (Xiu and Chai, 2014),
which consists of 31 state variables, including four nutrients [nitrate (NO_3), ammonium (NH_4), silicate, and
135 phosphate], three phytoplankton functional groups (representing picoplankton, diatoms and coccolithophorids), two
zooplankton classes (i.e., microzooplankton and mesozooplankton), four detritus pools (particulate organic
nitrogen/carbon, particulate inorganic carbon, and biogenic silica), four dissolved organic matters (labile and semi-
labile pools for both carbon and nitrate), and bacteria. The CoSINE model was successfully applied in the study on
the primary production (Liu and Chai, 2009), mesoscale eddy and its impacts (Guo et al., 2015), and the
140 phytoplankton community structure (Ma et al., 2013, 2014) in the SCS.

The physical modeled was initialized from a resting state with temperature and salinity specified using the World
Ocean Atlas (WOA2013, <https://www.nodc.noaa.gov/OC5/woa13/>) climatology. The initial distribution of nutrients
was also interpolated from the WOA climatological data. Small values were analytically assigned to other
ecosystem variables since the ecosystem module was insensitive to the initial conditions, except for nutrients. After
145 spinning up for 13 years with climatological forcing, the model was restarted with the ecosystem module driven by
interannually-varying CCMP wind and NCEP surface forcing from 2002 to 2011. The model outputs from 2005 to
2011 are analyzed.

2.4 Sensitivity Experiment

To quantify the contribution to ecosystem from coastal jet, we seek to control the coastal jet separation while
150 maintaining the larger basin-scale circulation. For the Vietnam boundary upwelling system, since nonlinear
advection is important to the separation of the coastal jet (Gan and Qu, 2008; Wang et al., 2006), an experiment
without the nonlinear advection terms in the momentum equations was conducted (e.g. Gruber et al. 2011). We note



that the advection terms in the tracer equations are retained for transport of active and passive tracers (i.e., ecosystem variables). Hereafter, this experiment will be referred as NO_ADV run.

155 3 Results

In this section, we first analyze the satellite-based observational data, focusing on the spatio-temporal covariance of wind, circulation, and biological production. After accessing the model performance against observation, we then describe and discuss the model results.

3.1 Spatio-temporal Analysis of Observation Data

160 Figure 2 shows mean (Fig. 2a) and standard deviation (Fig. 2b) of surface CHL overlaid with contours of mean ADT and KE respectively. In summer, the surface CHL has low concentration of $<0.1 \text{ mg m}^{-3}$ in the central SCS basin. By contrast, the CHL is more than fivefold ($>0.5 \text{ mg m}^{-3}$) along the southern Vietnamese coast. The high CHL water appears to extend offshore following the coastal jet to the interior SCS. The jet overshoots after separating from the coast and bifurcates into a northeastward current and a quasi-stationary anti-cyclonic eddy (Fig. 2a). Centered at $\sim 11^\circ$
165 N near the tip of Vietnamese coast, high KE ($>1.0 \text{ m}^2 \text{ s}^{-2}$) appears near the coast. The high variability of CHL coincides with KE into the interior SCS, implying the contribution from the jet (Fig. 2b).

The box-averaged (magenta box in Fig. 2b) time-series of monthly UI, KE and NPP are shown in Fig. 3a-c; they show seasonal and interannual variations. KE generally peaks in summer months, while NPP has a biannually signal, i.e., peaks in summer and winter, as well as complex non-seasonal signals. Unsurprisingly, UI dominates about half
170 ($R^2=0.4548$ for UI solely) of the total variability in NPP, which is consistent with studies in other wind-driven upwelling systems (Gruber et al., 2011). There are clear positive contributions to the biological production from both UI and KE. When KE is considered, additional $\sim 15\%$ of variability in NPP is explained ($R^2=0.6046$, $p<0.01$). Further investigation with 8-day mean NPP, UI, and KE after 60-day high pass filter also shows a similar and significant relationship (despite the correlation is lower, $R^2=0.1873$, $p<0.01$, not presented in figures), demonstrating
175 that the co-variation is robust not only for seasonal and longer time scales, but also for synoptic scale.

To further illustrate the modulation in the ecosystem by circulation, the high-NPP-anomaly (HNA) and low-NPP-anomaly (LNA) periods of currents were composited according to a non-seasonal NPP anomaly. The climatological signal was firstly removed from the summertime NPP, yielding the non-seasonal NPP anomaly. The thresholds for HNA and LNA are defined as (above) 75% and (below) 25% percentile of the NPP anomaly,
180 respectively. The velocity and direction for LNA, HNA and the normal state (i.e., neither LNA nor HNA) are respectively depicted in Fig. 4a-c, as well as the ADT difference between HNA and LNA (Fig. 4d). A student t-test suggests that the three circulation patterns are significantly ($p<0.01$) different. In contrast to the familiar separation and offshore jet pattern (Fig. 2a and Fig. 4c), the LNA circulation tends to flow along the coast without separation (Fig. 4a). On the other hand, the HNA circulation (Fig.4b) shows a clear separated jet and anticyclonic recirculating pattern south of the jet near 8.5° N , similar to the pattern seen during normal years (Fig. 4c); the flow speed is $\sim 20\%$
185



stronger than that of the normal state. Near the separation point, the HNA jet is more dissipated and slightly weakened compared with the LNA coastal jet. The KE averaged within the magenta box (Fig.2b) during the HNA state is $0.0827 \text{ m}^2 \text{ s}^{-2}$, which is ~65% larger than that during the LNA state ($0.0502 \text{ m}^2 \text{ s}^{-2}$). The difference in flow patterns is consistent with a dipolar ADT difference, by which a westward (inverse to the jet) pressure gradient force anomaly is imparted to the flow (Fig. 4d), which is responsible for the jet separation process (Batchelor, 1967; Gan and Qu, 2008). We now use model to address the physical-biogeochemical coupling.

3.2 Model Validation

In Fig. 5, simulated SST and NPP are compared with observations. The model reproduces reasonably well the observed patterns of SST and NPP. In particular, the model captures the cross-shore SST gradient. The cold filament that overshoots from the coast to the interior of SCS is also clearly reproduced by the model. However, the modeled SST shows a systematic cold bias of $\sim 1 \text{ }^\circ\text{C}$, and the modeled NPP does not simulate well the extreme high values ($>1000 \text{ mg C m}^{-2} \text{ d}^{-1}$) along the Vietnamese coast. This may in part be attributed to overestimation of retrieved NPP near the coast (e.g. Loisel et al., 2017). Off the coast, the model simulates well the crossshore gradient of productivity. The gradient is generally high in areas influenced by the jet.

Time series of modeled SST, surface KE and NPP, averaged over the magenta box (Fig.2b), are compared with observations in Fig. 6. Due in part to the realistic surface forcing and high resolution used, our model can reproduce the physical and biological parameters in the VBUS. The biannual signals in all three quantities agree reasonably well with the observations. At interannual time scales, during the 2010 El Niño event for example, monsoon was weaker (Fig. 3a), SST was warmer, and the KE was reduced. These features are simulated well, although the production drawdown is slightly weaker than the observation and the simulated SST under-estimates amplitude of the observed SST annual cycle by $\sim 1.0 \text{ }^\circ\text{C}$. For the surface current and productivity, our model shows excessive KE and insufficient production during winter, but the model-observation discrepancy is less notable in other seasons. The overestimated KE is partially contributed by the ageostrophic (e.g., Ekman) components in our modeled surface current. Nevertheless, we can conclude that our model reasonably reproduced the temporal variability in the VBUS.

In addition, vertical profiles of the simulated NO_3 and CHL, as two fundamental components of marine ecosystem, are compared with observations (Fig. 7). The modeled NO_3 generally reflects the oligotrophic condition near the surface and the nutricline approximately at 50 m. Below the nutricline, the NO_3 profile shows moderate vertical gradient to the deep. The simulated NO_3 profile matches the observations remarkably well. For the CHL, our model well simulates the concentration, not only at surface but also in the deep layer. Subsurface CHL maxima appears at $\sim 35 \text{ m}$, which is somewhat shallower than that in the observation. Both the modeled and observed CHL concentrations have large range from 0 to $>1.0 \text{ mg m}^{-3}$ in the subsurface CHL maxima. This reflects the large spatial variability in CHL.

Following the analysis in Sect. 3.1, the multi-variable regression analysis on the model outputs were also conducted. The modeled NPP presents a phase lag with respect to the UI and KE variation. When NPP is lagged for



220 one month, the correlation is 0.752 with a p -value of 0.0214, suggesting a significant regulation of the physical forcing to the productivity. Additionally, the composites of the HNA, LNA, and normal scenarios (Fig. 8) based on model outputs show contrasts among scenarios comparable to those in the observed cases in Fig. 4, further suggesting the reasonability of the model simulation.

225 In summary, one could find that our model performs reasonably in reproducing the key spatio-temporal features in the hydrodynamics and ecosystem of VBUS. Inevitably, some discrepancies exist, which are less evident in the summer months. Possible reasons for these discrepancies include insufficient horizontal resolution, unrealistic parameterizations (e.g., turbulent mixing), inaccuracy in the atmospheric forcing, or uncertainties in the ecosystem parameters. Nevertheless, considering current focus are to investigate the positive correlation between the productivity and the circulation, which was captured by the model (Fig. 8), these shortcomings are accepted.

230 3.3 Analysis of Model Results

Modeled circulation and potential density from the multi-summer average are presented in Fig. 9a-d, with sea surface height overlaid. Consistent with previous studies, the coastal current flows northward along the shelf (Hein et al., 2013). The current also dissipates freshwater from the Mekong River, while the water seldom spreads away from the coast. The coastal current veers at $\sim 11^\circ$ N, directs offshore and then separates, forming the quasi-stationary anticyclone centered at $\sim 110^\circ$ E, 9° N. Near the core of the anticyclone, vigorous vertical motion near surface can be found, implying submesoscale processes in play. Near 108° E, intensive onshore flow ascends on the slope. The high-density bottom water outcrops at 107° E, rejoining the coastal water and directing north, thus forming a circuit.

240 The biogeochemical variables reveal that the ecosystem is largely controlled by the circulation (Fig. 9e-h). Lateral nutrient gradient appears at the periphery of the anticyclone, which is characterized with depressed nitrate isosurface in the core and domed isosurface due to the upwelling and river injection near the coast (Fig. 9e). Stimulated by the river-injected and locally upwelled nutrient near the coast, primary production (PP) shows a surface maximum of $>30 \text{ mg C m}^{-3} \text{ d}^{-1}$ (Fig. 9g). The water with high production is then advected offshore by the jet (Fig. 9h), leading to an offshore bloom patch in curved shape which is familiar in the Vietnam coast (e.g., Fig. 5c). The jet also conveys the water with high particulate organic carbon (POC) offshore. The distribution of POC is somewhat deeper and more dissipated than that of high PP water, suggesting the vertical sinking and lateral transport processes (Nagai et al., 2015). Remineralization of POC results in a subsurface ammonium maximum at $\sim 50 \text{ m}$ (Fig. 9f) consistent with the study in SCS (Li et al., 2015). Part of the ammonium could then fuel nitrification and production, while the rest rejoins the circulation with the upwelling water in the bottom Ekman layer. In summary, the model outputs clearly reveal circuiting circulation and cycled ecosystem, which will be further discussed in Sect. 4.

250



4 Discussion

4.1 Biogeochemical Cycle in VBUS

Via analysis on satellite data and model outputs, consistent and robust positive contribution from the local circulation to the biological production was revealed, in addition to the contribution from the wind, in the summer
255 VBUS system. The contribution of the circulation is distinct from the major coastal upwelling systems, where the offshore transport by the mean current appears to suppress the production by reducing the nearshore nutrient inventory (Gruber et al., 2011; Nagai et al., 2015).

Comparing the ecosystems in LNA and HNA (Fig. 10), the following cycle can be deduced: (1) The upwelled and riverine input nutrient (majorly inorganic) stimulate high production near the Vietnam coast. (2) The produced
260 organic matters are transported offshore by the jet; The water has high CHL (e.g., Fig. 2a) and high organic matters in the euphotic zone; (3) A significant portion of the nutrient (majorly in organic form) is transported back to the south of VBUS by the westward recirculation. The quasi-stationary rotating anticyclone impedes further offshore leakage of the nutrients (Fig. 10). (4) The trapped organic matters are remineralized, forming the subsurface maxima of ammonium and replenishing the nitrate by nitrification. Afterwards, the nutrients are upwelled by bottom Ekman
265 pumping and wind-induced upwelling, and finally rejoin in the local biogeochemical cycle. The speed of this cycle plays a significant role in controlling the productivity.

4.2 Dynamic Analysis

By controlling the available nutrients, the circulation largely determines the speed of the biogeochemical cycle. The influence of the circulation is further elucidated below. Table 1 summarizes the difference of the ecosystems in the
270 standard run and NO_ADV experiment. The NO_ADV experiment can be regarded as an extreme case where the circulation shows very weak tendency of separation (also see Fig. A1). The horizontal and vertical fluxes of nitrate in three scenarios are also depicted in Fig. 11.

In the VBUS, the availability of nutrients principally controls the productivity (Hein et al., 2013). Considering a quasi-steady state of nutrient in a coastal region, river-injected and upward inputted nutrient should be counter-
275 balanced by vertical export production and lateral exchanges. The lateral exchanges include both advection and diffusion, while it was pointed out that horizontal mixing is one or two order-of-magnitude lower than that of horizontal advection (Lu et al., 2015). Hence, as a sink term, the lateral exchanges are determined mostly by the advective fluxes normal to the boundary of the predefined box. Diagnostic also suggests a dominance role of advection process in the vertical over mixing. Given the fact the standard run and NO_ADV experiment has the
280 same riverine input and similar export flux, one could infer that the difference between two model cases is largely due to the different lateral transports and upwelled fluxes of nutrients.

In the LNA (Fig. 4a and Fig. 8a) and also in the NO_ADV experiment (Fig. A1), the circulation pattern switches to the along-isobath pattern, which modifies the local biogeochemical cycle. More nutrient is transported northward



and offshore out of VBUS and never comes back, leading to a reduction of nutrient (Fig. 11). This effect can be demonstrated by cross-section nutrient flux across 109° E section. The more nutrient leakage, the less westward nutrient flux across this section. In NO_ADV run, the westward flux of nitrate is significantly reduced by 36.2% (Table 1). The reduction of nutrient is accompanied with suppressed the upward nutrient flux (-46.5 %) near the shelf edge (~100 m). As a consequence of more leakage and less upwelling influx, the nitrate reservoir and new production are significantly reduced by 20.7 % and 21.9 %, significantly inhibiting the primary production process (15.7 %, Table 1). Other ecosystem constituents decrease to a limit degree, such as -2.6% for ammonium, and -3.0% for DOC. This interpretation is further supported by the post-El Niño scenario. In 2010, more significant suppression occurs in the vertical nutrient flux (-99.6%), while the horizontal fluxes also respond to decrease. Due to the drawdown in the wind-induced upwelling and recirculation (Table 1), the production is extremely low in summer 2010 (Fig. 3c).

The more intensive separation, the larger KE in VBUS, and vice versa. The accelerated coastal current is also associated with intensified cross-isobath transport by bottom Ekman effect (Gan et al., 2009). Hence, high KE is linked to accelerated biogeochemical cycle. Combining all the effects, the intensified circulation is a condition favorable for the nutrient inventory, and hence the productivity, especially during relatively low KE scenarios.

5 Conclusions

Via analyzing the summertime remote sensing data in the VBUS, a tight spatio-temporal covariation between the ecosystem and near-surface circulation was revealed. The water with high kinetic energy appeared to coincide with high CHL variability. Statistical analysis suggested that high level of productivity was associated with high level of circulation intensity, which accounted for ~15% of the variability in productivity. Elevated kinetic energy and intensified circulation were related with the separation of the upwelling current system. Especially, in the low-productivity scenarios, the circulation pattern shifts from the intensive separation pattern to a moderate alongshore non-separated pattern.

To further investigate the linkage between the circulation and the ecosystem, a physical-biological coupled model was configured. Numerical experiment was designed to reproduce the non-separated circulation pattern, while maintaining the external monsoon forcing. The modeled results were validated favorably compared with the remote sensing and *in situ* observation data. In particular, model reproduced the positive contribution from the circulation intensity to the productivity.

Inspection into the model results highlighted the circulation's role in local biogeochemical cycle. As the schematic diagram in Fig. 12, the separated circulation and resultant quasi-stationary anticyclone were favorable for the recirculation of nutrients. During non-separation scenarios, the nutrients northward transported by the alongshore current would never come back, leading to a nutrient leakage. The nutrient leakage further induced the feedback summarized in Fig. 12b, which could reduce the nitrate inventory by ~21% and the NPP by ~16% in the experiment representative for very weak separation. The weakened coastal current was also associated with reduced bottom



Ekman transport, hence further reducing the vertical flux of nutrient. As the KE increasing, the biogeochemical cycle was accelerated. This resulted in the positive correlation to the productivity.

320 This finding provides a new insight into the complex physical-biological coupling in the Vietnam coastal upwelling system. Moreover, this understanding could help to predict the future reaction of productivity in the SCS. As revealed by Yang and Wu (2012), the summertime near-surface circulation of SCS had experienced a long-term trend of being more energetic, characterized with intensified separation and recirculation in the VBUS (see their figure 9). Whether this long-term trend of circulation will also induce potential trend in ecosystem in response to
325 future climate changes is a topic of common interests, which merits further investigation.

6 Data Availability

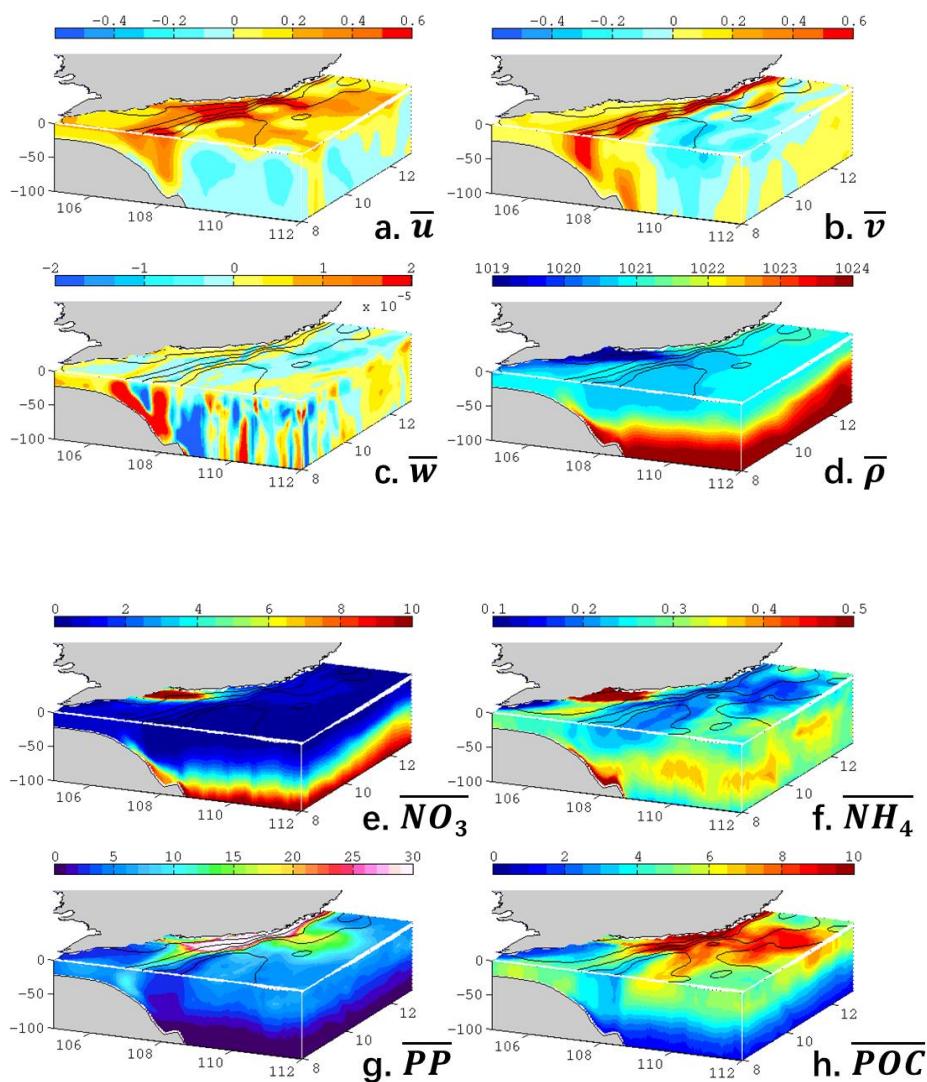
The CCMP gridded Ocean Surface Wind Vector L3.0 First-Look Analyses (Version 1) data was accessed [2015-03-12] at <http://dx.doi.org/10.5067/CCF30-01XXX>. The MODIS Aqua Level 3 CHL data was accessed [2014-05-16] at <http://oceancolor.gsfc.nasa.gov>. The VGPM NPP data was available at
330 <http://www.science.oregonstate.edu/ocean.productivity/index.php>. Gridded monthly-mean ADT, available at <http://www.aviso.altimetry.fr/en/data/products/sea-surface-height-products/global/>, was produced by Ssalto/Duacs (<http://www.aviso.oceanobs.com/duacs/>), and was distributed by Aviso with support from the Centre National d'Etudes Spatiales (*Cnes*). The OISST data was obtained from the National Climatic Data Center of NOAA (<https://www.ncdc.noaa.gov/oisst/data-access>).

335



Appendix A: Abbreviations

<i>Locations</i>		<i>Variables</i>	
SCS	South China Sea	CHL	chlorophyll-a
VBUS	Vietnam Boundary Upwelling System	NPP	vertical-integrated net primary production
<i>Data and Methods</i>		PP	primary production (as a function of depth)
CCMP	Cross-Calibrated Multi-Platform data	UI	upwelling intensity
MODIS	Moderate Resolution Imaging Spectroradiometer data	KE	kinetic energy
NCEP	National Centers for Environmental Prediction	POC	particulate organic carbon
VGPM	chlorophyll-based Vertically Generalized Production Model	<i>Modeling</i>	
ADT	Absolute Dynamic Topography	TFOR	Taiwan Strait Nowcast\Forecast system
OISST	Optimum Interpolation Sea Surface Temperature	CoSINE	Carbon, Silicon, Nitrogen Ecosystem model
HNA/LNA	high/low-NPP anomaly scenario	NO_ADV	model experiment with no advection term in momentum equations



340

345

Figure A1 Same with Fig. 9, but for NO_ADV model run. (a) Zonal velocity in m s^{-1} , (b) meridional velocity in m s^{-1} , (c) vertical velocity in m s^{-1} , (d) potential density in kg m^{-3} , (e) nitrate in mmol m^{-3} , (f) ammonium in mmol m^{-3} , (g) primary production in $\text{mg C m}^{-3} \text{d}^{-1}$, and particulate organic carbon in mmol C m^{-3} . Overlapped contours are the mean sea level (every 0.1 m).



Acknowledgements

350 This study was supported by grant No.2016YFA0601201 from the Ministry of Science and Technology of the People's Republic of China (MOST), and grants U1305231, 41476005, 41476007 and 41630963 from the National Natural Science Foundation of China (NSFC).

References

- 355 Atlas, R., Hoffman, R. N., Ardizzone, J., Leidner, S. M., Jusem, J. C., Smith, D. K., and Gombos, D.: A cross-calibrated, multiplatform ocean surface wind velocity product for meteorological and oceanographic applications, *Bull. Am. Meteorol. Soc.*, 92, 157-174, 2011.
- Batchelor, G. K.: *An Introduction to Fluid Dynamics*, Cambridge University Press, New York, 1967.
- Banzon, V., Smith, T. M., Chin, T. M., Liu, C., and Hankins, W.: A long-term record of blended satellite and in situ sea-surface temperature for climate monitoring, modeling and environmental studies. *Earth Syst. Sci. Data*, 8, 165–176, doi:10.5194/essd-8-165-2016, 2016.
- 360 Behrenfeld, M. J. and Falkowski, P. G.: Photosynthetic rates derived from satellite-based chlorophyll concentration, *Limnol. Oceanogr.*, 42, 1-20, 1997.
- Bryan, F. O., Hecht, M. W., and Smith, R. D.: Resolution convergence and sensitivity studies with North Atlantic circulation models. Part I: The western boundary current system, *Ocean Model*, 16, 141-159, 2007.
- 365 Chai, F., Liu, G., Xue, H., Shi, L., Chao, Y., Tseng, C.-M., Chou, W.-C., and Liu, K.-K.: Seasonal and interannual variability of carbon cycle in South China Sea: A three-dimensional physical-biogeochemical modeling study, *J. Oceanogr.*, 65, 703-720, 2009.
- Chen, G., Xiu, P., and Chai, F.: Physical and biological controls on the summer chlorophyll bloom to the east of Vietnam, *J. Oceanogr.*, 70, 323-328, 2014.
- 370 Chen, Z., Yan, X.-H., Jo, Y.-H., Jiang, L., and Jiang, Y.: A study of Benguela upwelling system using different upwelling indices derived from remotely sensed data, *Cont. Shelf Res.*, 45, 27-33, 2012.
- Dai, A., Qian, T., Trenberth, K. E., and Milliman, J. D.: Changes in continental freshwater discharge from 1948 to 2004, *J. Clim.*, 22, 2773-2792, 2009.
- 375 Dippner, J. W., Nguyen, K. V., Hein, H., Ohde, T., and Loick, N.: Monsoon-induced upwelling off the Vietnamese coast, *Ocean Dyn.*, 57, 46-62, 2006.
- Gan, J., Cheung, A., Guo, X., and Li, L.: Intensified upwelling over a widened shelf in the northeastern South China Sea, *J. Geophys. Res.*, 114, 2009.
- Gan, J. and Qu, T.: Coastal jet separation and associated flow variability in the southwest South China Sea, *Deep Sea Res. Part I*, 55, 1-19, 2008.
- 380 Griffies, S. M. and Hallberg, R. W.: Biharmonic Friction with a Smagorinsky-Like Viscosity for Use in Large-Scale Eddy-Permitting Ocean Models, *Monthly Weather Review*, 128, 2935-2946, 2000.
- Gruber, N., Lachkar, Z., Frenzel, H., Marchesiello, P., Munnich, M., McWilliams, J. C., Nagai, T., and Plattner, G.-K.: Eddy-induced reduction of biological production in eastern boundary upwelling systems, *Nature Geosci*, 4, 787-792, 2011.
- 385 Guo, M., Chai, F., Xiu, P., Li, S., and Rao, S.: Impacts of mesoscale eddies in the South China Sea on biogeochemical cycles, *Ocean Dyn.*, doi: 10.1007/s10236-015-0867-1, 2015. 2015.
- Hein, H., Hein, B., Pohlmann, T., and Long, B. H.: Inter-annual variability of upwelling off the South-Vietnamese coast and its relation to nutrient dynamics, *Global Planet. Change*, 110, 170-182, 2013.
- 390 Isoguchi, O. and Kawamura, H.: MJO-related summer cooling and phytoplankton blooms in the South China Sea in recent years, *Geophys. Res. Lett.*, 33, 2006.
- Jiang, Y. W., Chai, F., Wan, Z. W., Zhang, X., and Hong, H. S.: Characteristics and mechanisms of the upwelling in the southern Taiwan Strait: a three-dimensional numerical model study, *J. Oceanogr.*, 67, 699-708, 2011.
- Jiao, N., Zhang, Y., Zhou, K., Li, Q., Dai, M., Liu, J., Guo, J., and Huang, B.: Revisiting the CO₂ "source" problem in upwelling areas: a comparative study on eddy upwellings in the South China Sea, *Biogeosciences*, 11, 2465-395 2475, 2014.



- Kalnay, E., Kanamitsu, M., Kistler, R., Collins, W., Deaven, D., Gandin, L., Iredell, M., Saha, S., White, G., and Woollen, J.: The NCEP/NCAR 40-year reanalysis project, *Bull. Am. Meteorol. Soc.*, 77, 437-471, 1996.
- Kuo, N.-J., Zheng, Q., and Ho, C.-R.: Response of Vietnam coastal upwelling to the 1997–1998 ENSO event observed by multisensor data, *Remote Sens. Environ.*, 89, 106-115, 2004.
- 400 Kuo, N.-J., Zheng, Q., and Ho, C.-R.: Satellite observation of upwelling along the western coast of the South China Sea, *Remote Sens. Environ.*, 74, 463-470, 2000.
- Kuo, N. J. and Ho, C. R.: ENSO effect on the sea surface wind and sea surface temperature in the Taiwan Strait, *Geophys. Res. Lett.*, 31, 2004.
- Large, W. G., McWilliams, J. C., and Doney, S. C.: Oceanic vertical mixing: A review and a model with a nonlocal boundary layer parameterization, *Rev. Geophys.*, 32, 363-404, 1994.
- 405 Li, Q. P., Wang, Y., Dong, Y., and Gan, J.: Modeling long-term change of planktonic ecosystems in the northern South China Sea and the upstream Kuroshio Current, *J. Geophys. Res. Oceans*, 120, 3913-3936, 2015.
- Liao, E., Jiang, Y., Li, L., Hong, H., and Yan, X.: The cause of the 2008 cold disaster in the Taiwan Strait, *Ocean Model*, doi: 10.1016/j.ocemod.2012.11.004, 2013. 1-10, 2013.
- 410 Lin, X., Yan, X.-H., Jiang, Y., and Zhang, Z.: Performance assessment for an operational ocean model of the Taiwan Strait, *Ocean Model*, 102, 27-44, 2016.
- Liu, G. and Chai, F.: Seasonal and interannual variability of primary and export production in the South China Sea: a three-dimensional physical-biogeochemical model study, *ICES J. Mar. Sci.*, 66, 420-431, 2009.
- Liu, K.-K., Atkinson, L., Quinones, R., and Talaue-McManus, L.: Carbon and nutrient fluxes in continental margins: a global synthesis, Springer Science & Business Media, 2010.
- 415 Liu, K. K., Chao, S. Y., Shaw, P. T., Gong, G. C., Chen, C. C., and Tang, T. Y.: Monsoon-forced chlorophyll distribution and primary production in the South China Sea: observations and a numerical study, *Deep-Sea Research Part I-Oceanographic Research Papers*, 49, 1387-1412, 2002.
- Liu, W. T., Katsaros, K. B., and Businger, J. A.: Bulk parameterization of air-sea exchanges of heat and water vapor including the molecular constraints at the interface, *J. Atmos. Sci.*, 36, 1722-1735, 1979.
- 420 Liu, X., Wang, J., Cheng, X., and Du, Y.: Abnormal upwelling and chlorophyll-a concentration off South Vietnam in summer 2007, *J. Geophys. Res. Oceans*, 117, n/a-n/a, 2012.
- Loisel, H., Vantrepotte, V., Ouillon, S., Ngoc, D. D., Herrmann, M., Tran, V., Mériaux, X., Dessailly, D., Jamet, C., Duhaut, T., Nguyen, H. H., and Van Nguyen, T.: Assessment and analysis of the chlorophyll-a concentration variability over the Vietnamese coastal waters from the MERIS ocean color sensor (2002–2012), *Remote Sens. Environ.*, 190, 217-232, 2017.
- 425 Lu, W., Yan, X.-H., Han, L., and Jiang, Y.: One-dimensional ocean model with three types of vertical velocities: a case study in the South China Sea, *Ocean Dyn.*, doi: 10.1007/s10236-016-1029-9, 2017. 1-10, 2017.
- Lu, W., Yan, X.-H., and Jiang, Y.: Winter bloom and associated upwelling northwest of the Luzon Island: A coupled physical-biological modeling approach, *J. Geophys. Res. Oceans*, 120, 533-546, 2015.
- 430 Ma, W., Chai, F., Xiu, P., Xue, H., and Tian, J.: Modeling the long-term variability of phytoplankton functional groups and primary productivity in the South China Sea, *J. Oceanogr.*, 69, 527-544, 2013.
- Ma, W., Chai, F., Xiu, P., Xue, H., and Tian, J.: Simulation of export production and biological pump structure in the South China Sea, *Geo-Mar. Lett.*, 34, 541-554, 2014.
- 435 Nagai, T., Gruber, N., Frenzel, H., Lachkar, Z., McWilliams, J. C., and Plattner, G. K.: Dominant role of eddies and filaments in the offshore transport of carbon and nutrients in the California Current System, *J. Geophys. Res. Oceans*, 120, 5318-5341, 2015.
- Shchepetkin, A. and McWilliams, J.: The regional oceanic modeling system (ROMS): a split-explicit, free-surface, topography-following-coordinate oceanic model, *Ocean Model*, 9, 347-404, 2005.
- 440 Tang, D. L., Kawamura, H., Doan-Nhu, H., and Takahashi, W.: Remote sensing oceanography of a harmful algal bloom off the coast of southeastern Vietnam, *J. Geophys. Res. Oceans*, 109, 2004.
- Wang, G., Chen, D., and Su, J.: Generation and life cycle of the dipole in the South China Sea summer circulation, *J. Geophys. Res.*, 111, 2006.
- 445 Wang, J., Hong, H., Jiang, Y., Chai, F., and Yan, X.-H.: Summer nitrogenous nutrient transport and its fate in the Taiwan Strait: A coupled physical-biological modeling approach, *J. Geophys. Res. Oceans*, 118, 4184-4200, 2013.
- Wong, G. T. F., Ku, T. L., Mulholland, M., Tseng, C. M., and Wang, D. P.: The SouthEast Asian time-series study (SEATS) and the biogeochemistry of the South China Sea - An overview, *Deep Sea Res. Part II*, 54, 1434-1447, 2007.



- 450 Wyrski, K.: Physical Oceanography of the Southeast Asian waters. 1961.
Xie, S.-P., Hu, K., Hafner, J., Tokinaga, H., Du, Y., Huang, G., and Sampe, T.: Indian Ocean capacitor effect on Indo-western Pacific climate during the summer following El Niño, *J. Clim.*, 22, 730-747, 2009.
Xie, S. P., Xie, Q., Wang, D., and Liu, W. T.: Summer upwelling in the South China Sea and its role in regional climate variations, *J. Geophys. Res. Oceans*, 108, 2003.
- 455 Xiu, P. and Chai, F.: Connections between physical, optical and biogeochemical processes in the Pacific Ocean, *Prog. Oceanogr.*, 122, 30-53, 2014.
Xu, X., Qiu, Z., and Chen, H.: The general descriptions of the horizontal circulation in the South China Sea, 1982, 137-145.
- 460 Yang, H. and Wu, L.: Trends of upper-layer circulation in the South China Sea during 1959-2008, *J. Geophys. Res. Oceans*, 117, 2012.



Table

Table 1 Summary of the ecosystems in three model scenarios

Quantities integrated over top 100 m of the box region (Fig. 2b)	Standard	NO_ADV	2010 post-El Niño
NO ₃ ($\times 10^9$ mol)	11.3	8.96 (-20.7%)	10.71 (-5.2%)
NH ₄ ($\times 10^9$ mol)	1.52	1.48 (-2.6%)	1.51 (-0.7%)
DOC ($\times 10^9$ mol C)	234	227 (-3.0%)	236 (+0.9%)
POC ($\times 10^9$ mol C)	22.7	22.4 (-1.3%)	19.9 (-12.3%)
NPP (mmol N m ⁻² d ⁻¹)	4.65	3.92 (-15.7%)	3.57 (-23.2%)
New Production + Regeneration Production (mmol N m ⁻² d ⁻¹)	2.83+1.82	2.21+1.71 (-21.9%, -6.0%)	1.82+1.75 (-35.7%, -3.8%)
Fluxes			
Vertical NO₃ flux across 100 m level			
($\times 10^9$ mol d ⁻¹ , positive upward)	0.2454	0.1313 (-46.5%)	0.0011 (-99.6%)
Top 100 m integrated zonal NO₃ flux across 109° E section*			
($\times 10^9$ mol d ⁻¹ , positive westward)	0.4156	0.2652 (-36.2%)	0.2013 (-51.6%)
Vertical volume flux across 100 m level (Sv, positive upward)			
	0.22	0.14 (-36.4%)	0.04 (-81.8%)
Top 100 m integrated zonal volume flux across 109° E section* (Sv, positive westward)			
	0.44	0.01 (-97.7%)	0.28 (-36.4%)

* See Fig. 11a for the location.



Figures

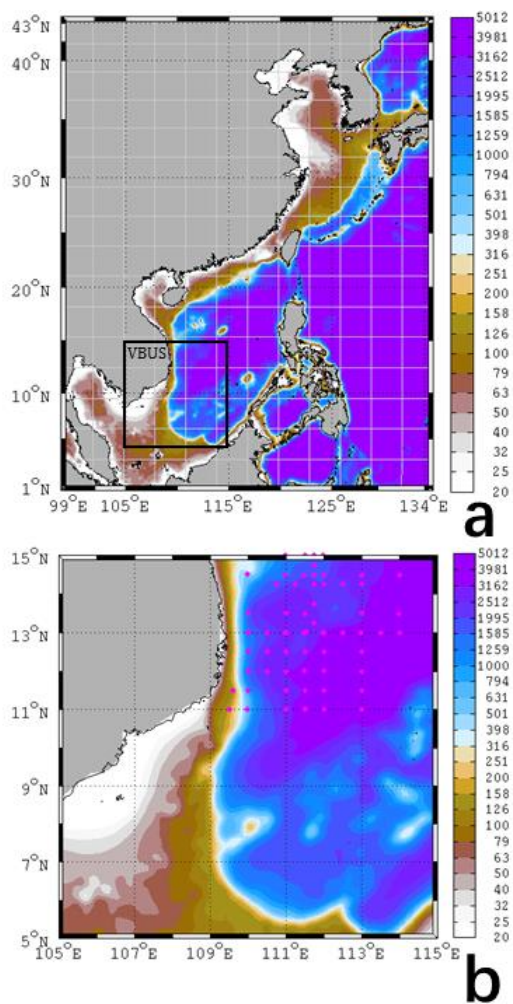
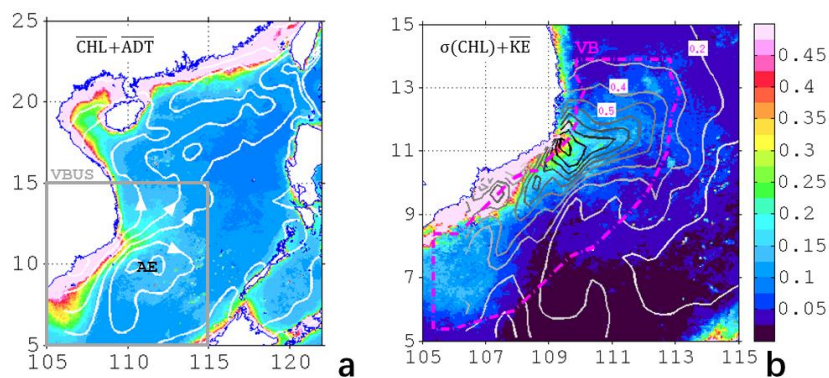


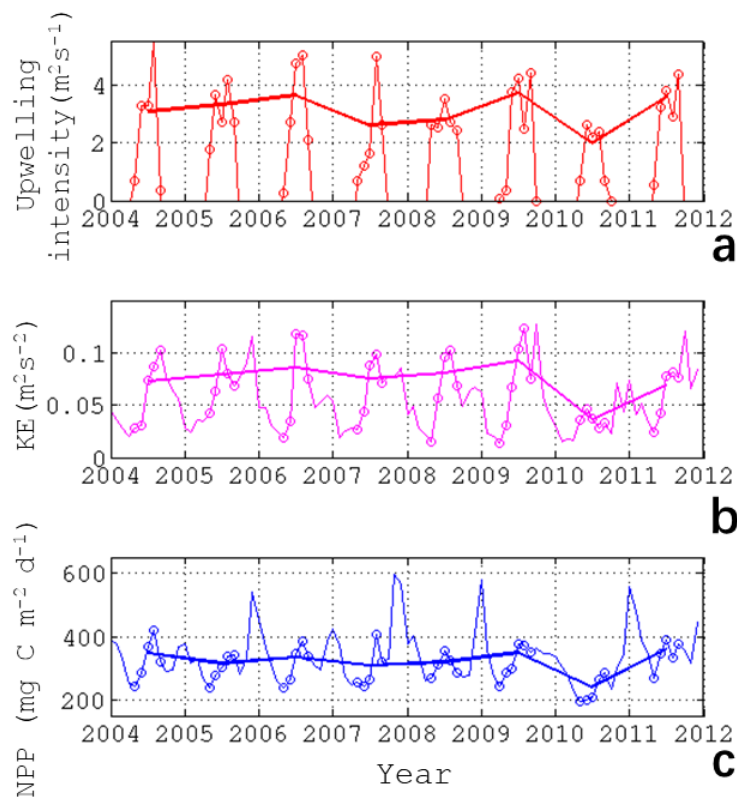
Figure 1 (a) Model domain and the bathymetry (unit: meter) for the TFOR-CoSINE model. Model grid nodes are shown every 25 points. The study area VBUS is boxed. (b) Zoom-in area of VBUS. Magenta diamonds are the observation stations (see text).

470

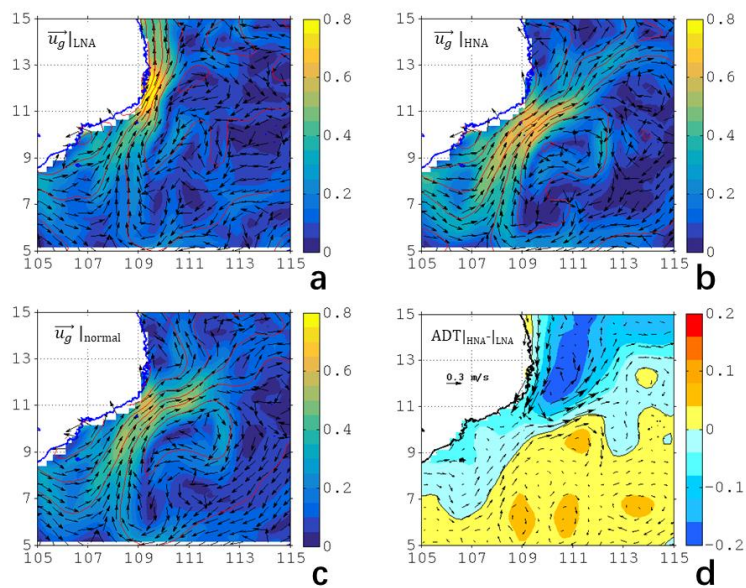


475

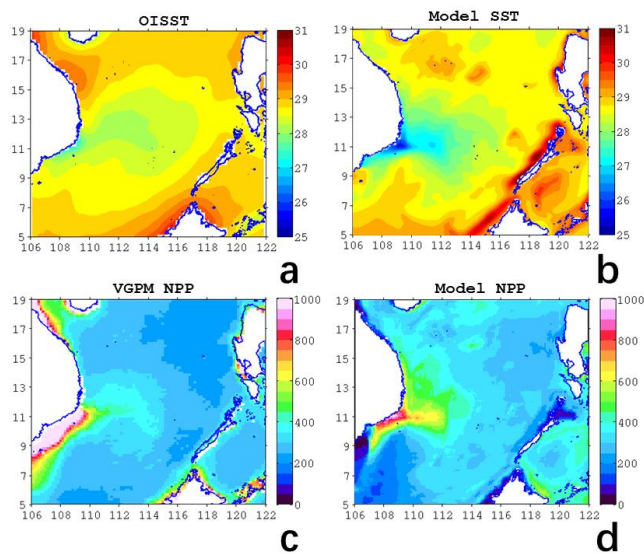
Figure 2 (a) Summertime (MJAS) average of surface CHL concentration (color shading, unit: mg m^{-3}) from MODIS, overlapped white contours are mean ADT with the arrows showing the directions of geostrophic currents. Gray box is the region of interest (VBUS), while AE shows the center of the anticyclone. (b) Standard deviation of surface CHL (color shading, unit: mg m^{-3}) overlapped with the contours of surface KE with an interval of 0.1 from 0.1 to 1.0 (unit: $\text{m}^2 \text{s}^{-2}$). Magenta box is the box region (see text).



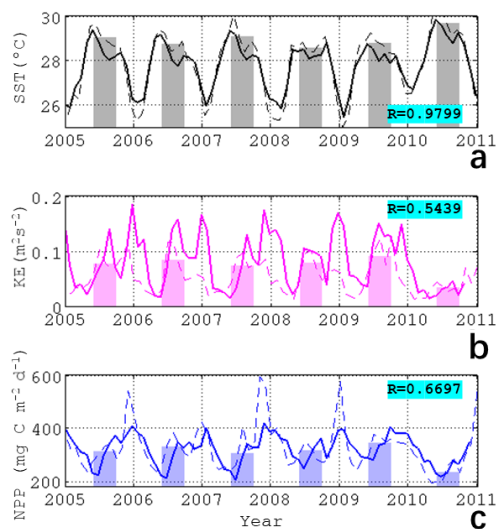
480 **Figure 3** Time series of (a) UI in $\text{m}^2 \text{s}^{-1}$, (b) KE in $\text{m}^2 \text{s}^{-2}$ and (c) NPP in $\text{mg C m}^{-2} \text{d}^{-1}$ of monthly data (thin lines) and summer mean (thick lines). In (a), only the positive (upwelling-favorable) values are shown. Months with positive UI are marked with open circles.



485 **Figure 4** The surface geostrophic current velocity (color shading, unit: m s^{-1}), direction (vectors), and respective ADT (red contours, unit: meter) in LNA (a), HNA (b), and normal months (i.e., neither LNA nor HNA, c) scenarios (see text for criteria). (d) The differences of ADT and geostrophic current between HNA and LNA.



490 **Figure 5 (a) OISST and (b) model SST (unit: °C), (c) VGPM NPP and (d) modeled NPP (unit: $\text{mg C m}^{-2} \text{d}^{-1}$) in multi-year August average.**



495 **Figure 6** Thick lines: modeled (a) SST in °C, (b) KE in $\text{m}^2 \text{s}^{-2}$, and (c) NPP in $\text{mg C m}^{-2} \text{d}^{-1}$ averaged over the box region (see Fig. 2b), with respective observation data (thin dashed lines) and their summer mean (bar). Correlation coefficients are also show in each plot.

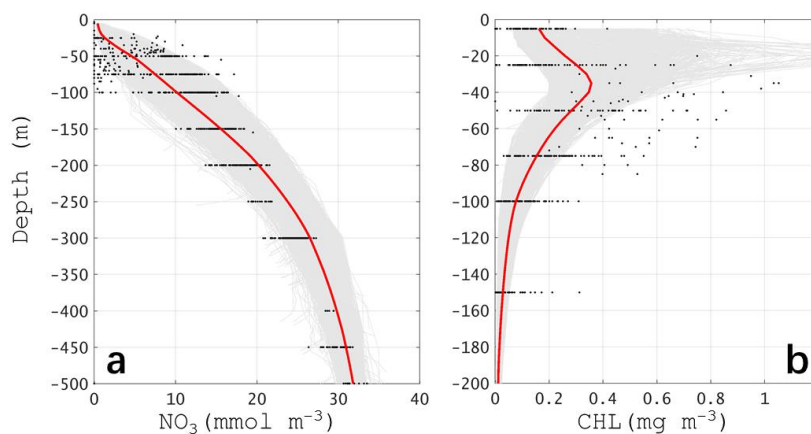


Figure 7 The vertical profiles of (a) nitrate concentration (unit: mmol m^{-3}) and (b) CHL concentration (unit: mg m^{-3}). In both plots, the black dots are the observation values (see Fig. 1b for stations). The gray area are the envelop for all model stations in the same area and month, while the red lines are the area-mean profiles.

500

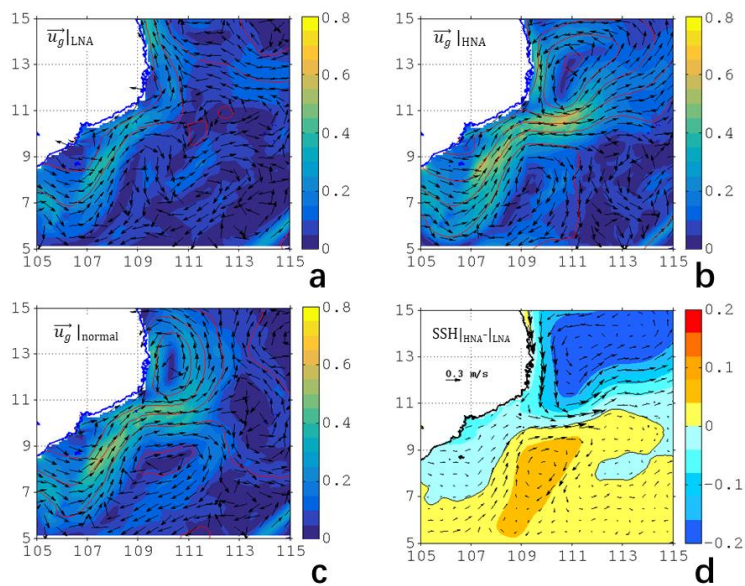
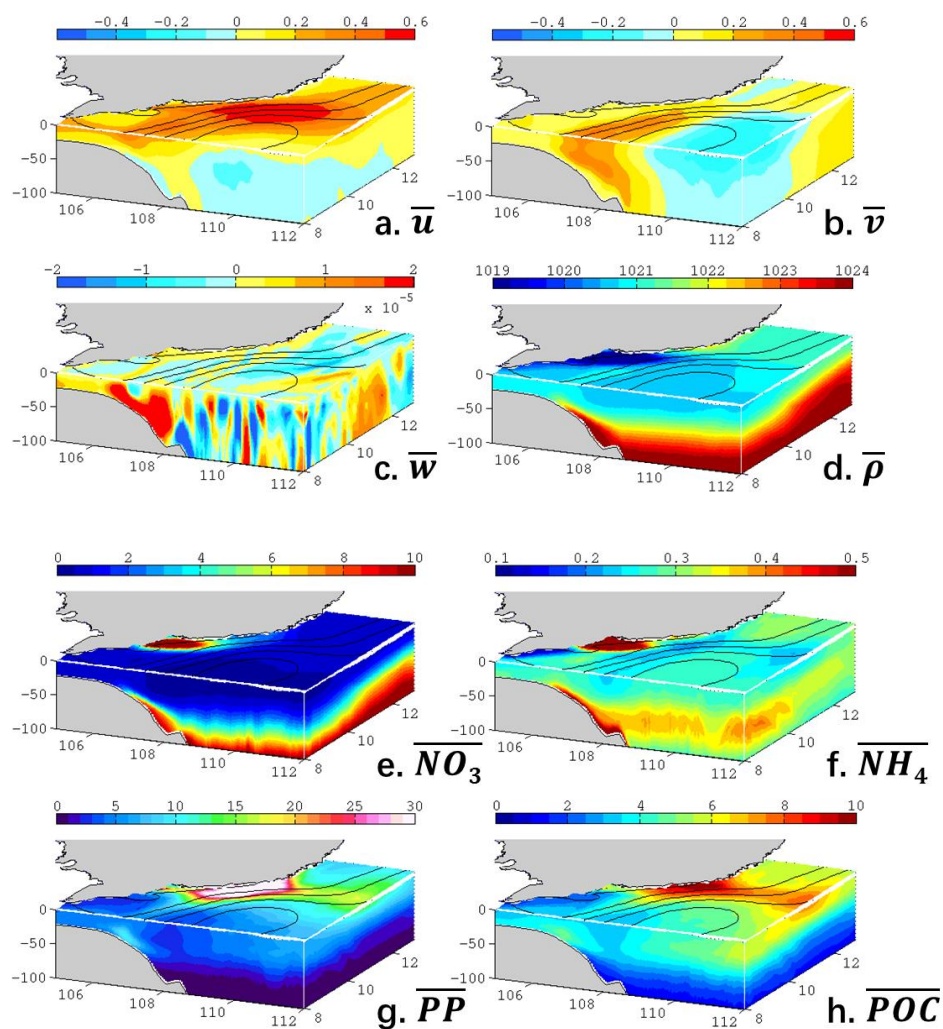


Figure 8 Same with Fig. 4, but based on model outputs.

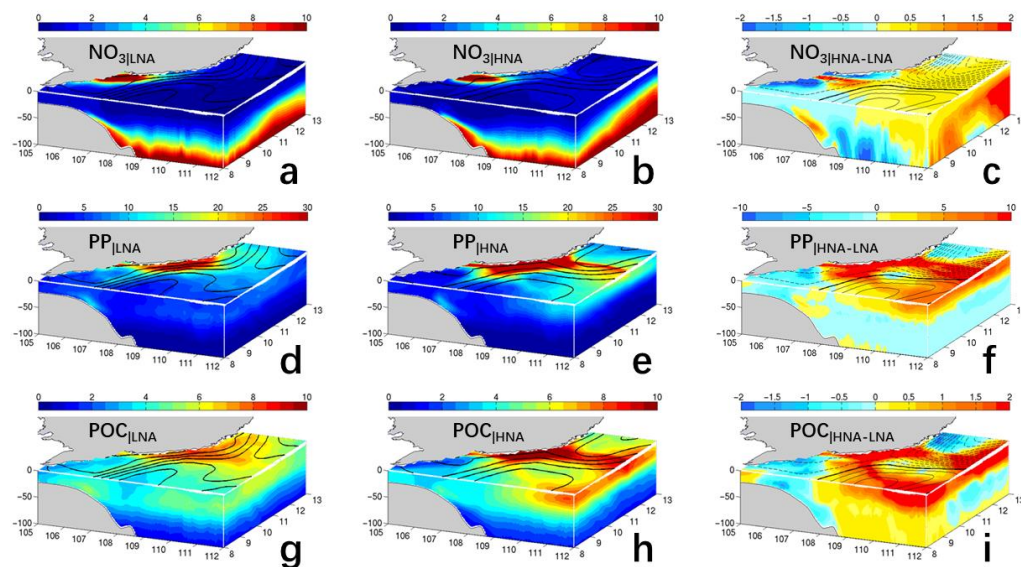


505

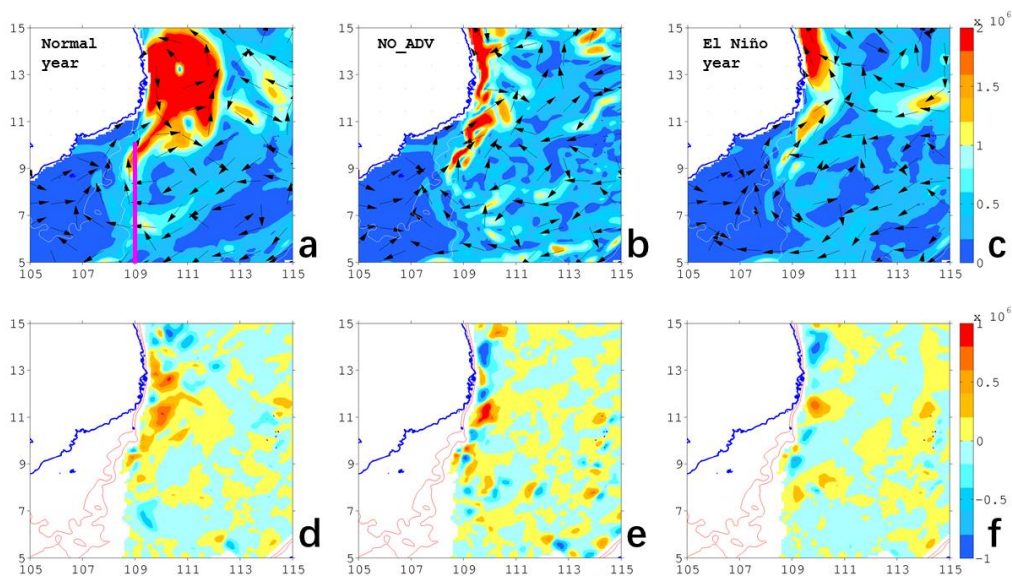


510

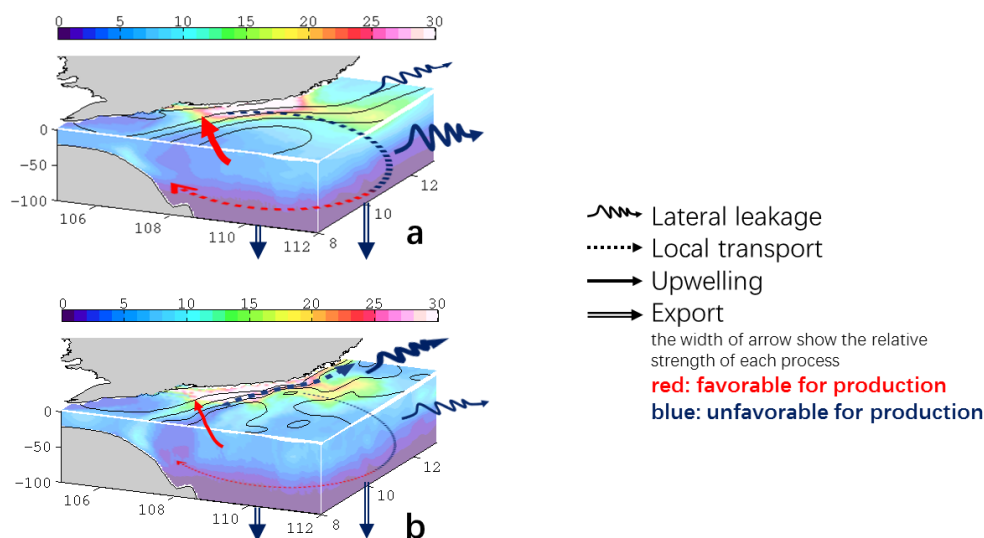
Figure 9 Three-dimensional distribution (standard run) of the summer mean (a) zonal velocity in m s^{-1} , (b) meridional velocity in m s^{-1} , (c) vertical velocity in m s^{-1} , (d) potential density in kg m^{-3} , (e) nitrate in mmol m^{-3} , (f) ammonium in mmol m^{-3} , (g) primary production in $\text{mg C m}^{-3} \text{d}^{-1}$, and particulate organic carbon in mmol C m^{-3} . Overlapped contours are the mean sea level (every 0.1 m).



515 **Figure 10** Modeled NO_3 (first row, in mmol m^{-3}), PP (second row, $\text{mg C m}^{-3} \text{d}^{-1}$) and POC (third row, mmol C m^{-3}) distribution in LNA (left column), HNA (middle column) and the difference between two scenarios (right column). See text for the definition of LNA and HNA.



520 **Figure 11 (Upper) Modeled 0-100 m integrated nitrate fluxes (unit: mmol s⁻¹) in horizontal plane. Color shading is the magnitude while vectors denote the direction. (Lower) Vertical flux across 100 m level for normal year (a and d), NO_ADV case (b and e), and post-El Niño (c and f). Overlapped contours are the 50 m and 75 m isobath. In (a), the magenta line is the 109° E section (Table 1).**



525 **Figure 12 Schematic diagram summarizing the dynamics in different scenarios of distinct circulation pattern in the VBUS,**
overlapped with the three-dimensional distribution of PP (unit: mg C m⁻³ d⁻¹). (a) Normal state: The separated jet
530 transports the upwelled nutrient and produced organic matter offshore. While a substantial portion of the offshore
transported organic matter leaks into the interior of SCS and never comes back, the recirculation and quasi-stationary
anticyclonic eddy trap the organic matters locally, and hinder further leakage of available nutrients in VBUS. The locally
recirculated nutrient is then upwelled in the bottom Ekman layer, rejoining the production process over the shelf. (b)
Non-separation state: During the non-separated circulation, the along-isobath circulation transports the organic matter
northward. The leakage of organic matter reduces the nutrient inventory in the VBUS. The loss of nutrients diminishes
the nutrient inventory available for remineralization and upwelling, further inducing a reduction in the production
process.

535